methods

Morphology and structure of lipoproteins revealed by an optimized negative-staining protocol of electron microscopy

Lei Zhang,[1,*,†] James Song,[1,†] Giorgio Cavigiolio,[§] Brian Y. Ishida,[**] Shengli Zhang,[††] John P. Kane,[**] Karl H. Weisgraber,[§§] Michael N. Oda,[§] Kerry-Anne Rye,[*,†††,§§§] Henry J. Pownall,[****] and Gang Ren[2,*,†,††]**

Molecular Foundry,* Lawrence Berkeley National Laboratory, Berkeley, CA 94720; Department of Biochemistry and Biophysics,† University of California, San Francisco, CA 94158; Children's Hospital Oakland Research Institute,§ Oakland, CA 94609; Cardiovascular Research Institute,** University of California, San Francisco, CA 94158; Department of Applied Physics, Xi'an Jiaotong University,†† Xi'an 710049, China; Gladstone Institute of Neurological Disease and Department of Pathology,§§ University of California, San Francisco, CA 94158; Lipid Research Group, The Heart Research Institute,*** Sydney, NSW 2050, Australia; Faculty of Medicine, University of Sydney,††† NSW 2060, Australia; Department of Medicine,§§§ University of Melbourne, VIC 3010, Australia; and Department of Medicine,**** Baylor College of Medicine, Houston, TX 77030

Abstract Plasma lipoprotein levels are predictors of risk for coronary artery disease. Lipoprotein structure-function relationships provide important clues that help identify the role of lipoproteins in cardiovascular disease. The compositional and conformational heterogeneity of lipoproteins are major barriers to the identification of their structures, as discovered using traditional approaches. Although electron microscopy (EM) is an alternative approach, conventional negative staining (NS) produces rouleau artifacts. In a previous study of apolipoprotein (apo)E4-containing reconstituted HDL (rHDL) particles, we optimized the NS method in a way that eliminated rouleaux. Here we report that phosphotungstic acid at high buffer salt concentrations plays a key role in rouleau formation. We also validate our protocol for analyzing the major plasma lipoprotein classes HDL, LDL, IDL, and VLDL, as well as homogeneously prepared apoA-I-containing rHDL. High-contrast EM images revealed morphology and detailed structures of lipoproteins, especially apoA-I-containing rHDL, that are amenable to three-dimensional reconstruction by single-particle analysis and electron tomography.—Zhang, L., J. Song, G. Cavigiolio, B. Y. Ishida, S. Zhang, J. P. Kane, K. H. Weisgraber, M. N. Oda, K-A. Rye, H. J. Pownall, and G. Ren. **The morphology and structure of lipoproteins revealed by an optimized negative-staining protocol of electron microscopy. *J. Lipid Res.* 2011.** 52: **175–184.**

Supplementary key words lipoprotein structure • lipoprotein morphology • protocol

Plasma cholesterol is transported by lipoproteins, macromolecular assemblies of proteins and lipids. A high plasma total cholesterol level is a risk factor for heart disease (1). Lipoproteins consist of a neutral lipid core surrounded by an outer shell of phospholipids and amphipathic apolipoproteins that confer water solubility on the lipid constituents (2). Lipoproteins are classified according to their densities as high-, low-, intermediate-, and very-low-density lipoproteins (HDL, LDL, IDL, and VLDL, respectively), as well as chylomicrons (3); HDL and LDL are major players in plasma cholesterol metabolism.

LDL can undergo oxidative modifications that mediate the accretion of LDL cholesterol in the arterial wall. LDL particles vary in size, shape, and composition (4, 5) and comprise large LDL (LDL1–2) and small, dense LDL (LDL3–7) subclasses (6); the latter are more prone to

This work was supported by the Office of Science, Office of Basic Energy Sciences of the U.S. Department of Energy (contract no. DE-AC02-05CH11231) and the W. M. Keck foundations to G.R. L.Z. was supported in part by the State Scholarship of China through China Scholarship Council (file no. 2008628018).

✤ ***Author's Choice**—Final version full access.*

Manuscript received 4 September 2010 and in revised form 20 October 2010.

Published, JLR Papers in Press, October 26, 2010
DOI 10.1194/jlr.D010959

Abbreviations: apo, apolipoprotein; CE, cholesteryl ester; cryoEM, cryo-electron microscopy; cryo-NS, cryo-negative-staining; DPBS, Dulbecco's phosphate-buffered saline; EM, electron microscopy; IDL, intermediate density lipoprotein; NS, negative staining; NS-EM, negative-staining electron microscopy; PTA, phosphotungstic acid; RCT, reverse cholesterol transport; rHDL, reconstituted HDL; UC, unesterified cholesterol; UF, uranyl formate.

[1] L. Zhang and J. Song contributed equally to this work.

[2] To whom correspondence should be addressed.
email: gren@lbl.gov

[S] The online version of this article (available at http://www.jlr.org) contains supplementary data in the form of two figures.

oxidation (6). Each LDL particle contains one molecule of apolipoprotein B-100 (apoB-100), a ligand for hepatic clearance of plasma cholesterol via LDL receptors (7).

HDL sequesters cholesterol from peripheral tissues, including the arterial wall, and transports it to the liver for recycling and disposal, a process called reverse cholesterol transport. HDL subspecies comprise particles that vary in size, shape, and composition (4, 8). They distribute according to size and surface charge into pre-β and α particles (including HDL_{3a}, HDL_{3b}, HDL_{3c}, HDL_{2a}, and HDL_{2b}) (9). HDL particles contain multiple apolipoproteins. The most abundant apolipoprotein is apoA-I, which mediates cholesterol efflux via cellular ATP-binding cassette transporter A1 (ABCA1). This process produces nascent discoidal HDL particles (10) which are converted to spherical HDL by lecithin-cholesterol acyltransferase (LCAT) (11). Spherical HDL are the dominant form of HDL in plasma and are hepatically removed by scavenger receptor class B type I (SR-BI), which mediates selective cholesteryl ester uptake (12). Reconstituted HDL (rHDL) particles consisting of apoA-I with various amounts of phosphatidylcholine and unesterified cholesterol (UC) have been used to develop new structure–function relationships (13). These particles can be converted to spherical rHDL by LCAT and LDL, which provide unesterified cholesterol for the reaction (14).

HDL particles in vivo vary in size, shape, components, and biological functions (15, 16). Determination of the structure of HDL particle is frustrated by their heterogeneity and dynamic nature (17-19). Electron microscopy (EM) is a powerful tool allowing direct visualization of individual particles (20, 21). Although frozen-hydrated lipoproteins can be viewed by cryo-electron microscopy (cryoEM) without distorting stains or fixatives (5), contrast is limited. Contrast can be enhanced by classification and averaging methods in which thousands of images are collected, grouped, and averaged based on similarity (cross-correlation coefficient) between each two images (22, 23). However, this strategy fails for heterogeneous particle populations (21). Conventional negative staining EM (NS-EM), an easy, rapid, and qualitative method for structural analysis of organelles and macromolecules, involves deposition of heavy metal stains on targets and provides better contrast and resistance to radiation damage than cryoEM. Although the resulting high-contrast images might better reveal structural details, there may also be stain-induced structural artifacts, including the formation of rouleau.

As a proof of concept, we developed a new NS-EM method that minimizes the rouleau formation usually seen in NS-EM studies and used this approach to report structural analysis of apoE4•1-palmitoyl-2-oleoyl phosphatidylcholine (POPC) rHDL (21). The NS-EM images were similar to cryoEM images but had better contrast. This approach enabled individual lipoprotein particles to be better visualized, measured, and classified into homologous particles, which are suitable for high-resolution three-dimensional (3D) reconstruction. Here we report the effects of different conditions on rouleau formation based on POPC liposome vesicles. The resulting optimized NS-EM protocol was then used to identify the chemical basis of rouleau formation and to examine whether this approach could be used to visualize several subclasses/subspecies of lipoproteins.

MATERIALS AND METHODS

Preparation of apoA-I-containing rHDL subclasses of discoidal 7.8-nm, 8.4-nm, 9.6-nm, and spherical 9.3-nm rHDL

Human apoA-I was expressed in *Escherichia coli* and isolated by Hi-Trap nickel affinity chromatography as described previously (24). Discoidal rHDL was reconstituted from apoA-I, POPC, and UC as described previously (14). Multiple rHDL subclasses were generated from affinity purified apoA-I by using different POPC/UC/apoA-I molar ratios. rHDL particles of 7.8 and 8.4 nm (diameter) were produced from a 30:2:1 (mol/mol/mol) molar ratio of POPC/UC/apoA-I; 9.6-nm (diameter) rHDL were obtained at a POPC/UC/apoA-I molar ratio of 80:4:1. More homogeneous particles were isolated by size-exclusion chromatography (14) and stored in Tris-buffered saline (TBS) (8.2 mM Tris, 150 mM NaCl, 1 mM EDTA, pH 8.0) (supplementary Fig. IA).

ApoA-I spherical 9.3-nm-diameter rHDL particles were isolated and purified from pooled samples of human plasma, as reported previously (25). In brief, spherical 9.3-nm rHDL was generated by incubating rHDL (POPC/UC/apoA-I molar ratio of 100:10:1) with fatty acid-free BSA, β-mercaptoethanol, LDL, and LCAT (26). The resulting spherical rHDL (supplementary Fig. IB) were isolated by sequential ultracentrifugation in the density (d) range of 1.07–1.21 g/ml (26).

Production of POPC liposome vesicles

POPC liposome vesicles were ordered from Encapsula NanoSciences. POPC liposome vesicles containing 1 mg/ml POPC with peak vesicle size of ~50 nm were produced and isolated in a buffer containing 20 mM Tris-Cl, 154 mM NaCl, pH 7.4.

Isolation of HDL from human plasma

HDL from plasma of fasting, healthy, normocholesterolemic male volunteers was isolated by sequential KBr density gradient ultracentrifugation from EDTA-plasma at densities of 1.063 and 1.21 g/ml, as described previously (27). α-Migrating apoA-I containing lipoproteins was isolated from EDTA-plasma by anti-apoA-I immuno-affinity chromatography. ApoA-I containing lipoproteins was subjected to preparative agarose electrophoresis (0.8%, w/v; Bio-Rad) at 3°C in buffer containing 62 mM Tris, 27 mM tricine, 5 mM calcium lactate, and 0.025% sodium azide and recovered from the gel by electroelution in the same buffer. Further purification was accomplished by Superdex 200 chromatography (supplementary Fig. IC). HDL α-migration was characterized by 2D (agarose nondenaturing) PAGE and then resolved on the basis of charge in the first dimension by flatbed agarose zonal electrophoresis (250 V, 10°C) before being resolved by size (Mini-Protean II; 3,000 V-h, 10°C; Bio-Rad) in 4%–30% nondenaturing gradient gel electrophoresis using a buffer system consisting of 25 mM Tris, 192 mM glycine-HCl, 1 mM EDTA, pH 8.3. Stokes diameters were determined by reference to high-molecular weight calibrators (GE Healthcare) supplemented with LDL (range, 1.030–1.050 g/ml) (25 nm) and ovalbumin (6.0 nm).

Isolation of LDL, IDL, and VLDL from human plasma

LDL ($1.019 < d < 1.063$ g/ml), IDL ($1.006 < d < 1.019$ g/ml), and VLDL ($d < 1.006$ g/ml) were isolated by sequential flotation

of plasma from a fasted, healthy male volunteer and further purified by isopycnic density gradient ultracentrifugation as described previously (28). LDL3 (d = 1.043 g/ml) was collected and dialyzed vs. TBS (10 mM Tris, 100 mM NaCl, 0.5 mM EDTA, pH 7.4) (supplemental Fig. ID). Protein concentration was determined with a detergent compatible (DC) protein assay (Bio-Rad) using BSA as a standard. LDL, IDL, and VLDL were stored at 4°C under nitrogen gas and used within 14 days of isolation (28).

Preparation of specimens for NS-EM using the conventional protocol

Lipoproteins (0.1 mg/ml protein) and 2% sodium phosphotungstate (pH 7.4 in deionized water) were mixed 1:1 (v/v) and sonicated as described previously (29), and ~4 μl was placed on a glow-discharged carbon-coated grid and allowed to sit for 60 s. Excess solution was removed by touching a piece of filter paper to the back of the grid.

Preparation of specimens for NS-EM using the optimized protocol

The NS-EM protocol was performed as described previously (21). Briefly, a 2.5-μl drop of lipoprotein solution (0.005 mg/ml protein) was placed on a glow-discharged thin carbon-coated 300-mesh copper grid (Cu-300CN; Pacific Grid-Tech, San Francisco, CA). After ~1 min, the excess solution was removed by blotting with filter paper. The grid was washed by briefly touching the surface of the grid with a drop (~30 μl) of deionized water on Parafilm and then blotted dry with filter paper. The touching and blotting steps were performed three times, each with a clean drop of deionized water. Three successive drops (~30 μl/drop) of 1% (w/v) uranyl formate (UF) (pH 4.6) solution were applied on Parafilm, and the excess solution was removed by blotting similarly. The grid remained in contact with the last UF drop with the sample side down for 1–3 min in the dark before excess stain was removed and the sample was air dried at room temperature (21). Since UF is light-sensitive and unstable, new solutions were divided into aliquots stored in small tubes at –80°C. Just before use, a tube of aliquot was thawed in the dark and filtered (0.02-μm filter) with the filter syringe wrapped in aluminum foil to exclude light.

Preparation of specimens for Cryo-NS-EM

Specimens for cryo-NS-EM were prepared as described previously (30) with modifications (21). Briefly, rHDL were diluted to a final protein concentration of 0.01 mg/ml with Dulbecco's PBS (DPBS) (2.7 mM KCl, 1.46 mM KH_2PO_4, 136.9 mM NaCl, and 8.1 mM Na_2HPO_4; Invitrogen, Carlsbad, CA), and a drop (3 μl) of lipoprotein solution was applied to a glow-discharged holey carbon film-coated 400-mesh grid (Quantifoil Micro Tools, Jena, Germany) for 1 min. The grid was washed with deionized water droplets and 1% UF. Samples were blotted with filter paper on both sides for 2 s at 100% humidity at 4°C with an Philips Electron Optics/FEI Vitrobot (FEI Company, USA), rapid-plunging device and then flash-frozen in liquid ethane.

EM data collection

NS-EM and cryo-NS-EM specimens were examined with an FEI Tecnai 20 or T12 transmission electron microscope operating at 200 kV or 120 kV. For cryo-NS-EM specimens, micrographs were acquired with a Gatan UltraScan 4K x 4K charge-coupled device camera at a magnification of 80,000× (Tecnai 20). Micrographs were obtained at −180°C with a Gatan cryo-holder under low-electron-dose conditions in which each micrograph pixel corresponded to 0.14 nm. The same conditions were used for obtaining NS-EM micrographs, except without the cryo-holder and not in low-electron-dose mode. The T12 EM was operated at a magnification of 67,000×, with each pixel of the micrographs corresponding to 0.17 nm.

Image processing

Images were processed with several software suites (EMAN, SPIDER, FREALIGN). The contrast transfer function parameters for each micrograph were determined with *ctffind3* in FREALIGN (31) and corrected with SPIDER software (23). Particles were automatically selected with the *e2boxer.py* program in EMAN2 (32) and then manually extracted with the *boxer* program in the EMAN package (22).

Statistical analysis

For morphometric analysis, individual particle images were selected with *e2boxer.py* in EMAN2 (32). Particles were picked automatically and manually checked to remove overlapping or damaged particles with boxer software (22). More than 200 particle images from micrographs of each condition were used for statistical analysis of particle size distribution. Particle size was determined by measuring diameters in two orthogonal directions, one of which was the longest dimension. The geometric mean of the perpendicular diameters was used to represent the particle size/diameter. The aspect ratio of the long and the perpendicular diameters was used to represent particle shape. Histograms of particle diameters were generated with 0.5 nm sampling steps for rHDL/HDL subfractions and with 1.0 nm for LDL, IDL, and VLDL. After normalization, each histogram was fitted with a 9th degree polynomial function in Matlab for data analysis. Histograms of particle ratios were computed and fitted in the same manner as particle sizes were but with a 0.1-sampling step for rHDL/HDL subfractions and a 0.05 step for LDL, IDL, and VLDL.

Reference-free classification and averaging

To reduce image noise and enhance clarity, a 2D reference-free class-averaging program was used to analyze particle variation (33). Class-averaging of the particle images used a classification algorithm to quantify similarities among different particle images. Images containing high cross-correlation values were grouped together, aligned to each other, and then averaged for improving the signal-to-noise ratio. In our experiment, particle images from each HDL subclass/subfraction (9,703 9.6-nm rHDL; 6,841 8.4-nm rHDL; 5,578 7.8-nm rHDL; 17,441 NS 9.3-nm spherical rHDL; and 5,386 cryo-NS 9.3-nm spherical rHDL) were selected from micrographs and extracted as 160- × 160-pixel images by using *boxer* software (22). Particle images were normalized after X-ray sparkles were filtered out. A circular mask with a Gaussian boundary was applied to all images before classification. By using *refine2d.py* software (EMAN package) for four iterations (22), images were separated into more than 500 groups/classes based on their cross-correlation coefficients, and then images in each group were aligned to each other and averaged together to enhance the signal and reduce the noise (22).

RESULTS

Rouleau formation in NS of lipoproteins is an artifact

With conventional NS-EM protocols (34, 35), particles stack into rouleaux formation (36-41). Both the 9.6-nm discoidal apoA-I rHDL (supplementary Fig. IIA) and the apoB-100 LDL (supplementary Fig. IIC) appeared as rouleaux, similar to those observed with apoE4 rHDL (21). Within the rouleau, particles were separated by dark

boundaries, and their surfaces were flattened and parallel to each other, with the longest diameter of each particle roughly perpendicular to the central axis of the rouleau (supplementary Fig. IIB, D). Rouleau formation was not related to particle concentration because they were also apparent at low-particle concentrations (data not shown).

Evidence that rouleau formation is an artifact of the conventional NS-EM protocol comes from results for nondenaturing polyacrylamide gradient gel electrophoresis and cryoEM studies (2, 4, 8, 21, 42), where apoA-I rHDL, apoE4 rHDL, and LDL all appear as distinct particles without stacking. Mass spectrometric (2, 18) and small-angle X-ray diffraction data (43) are also consistent with single particles, further suggesting that rouleau formation is an artifact of the NS-EM protocol.

NS-EM of LDL, 9.6-nm apoA-I rHDL, and apoE4 rHDL share three conditions, one or more of which might induce rouleau formation: *i*) phosphotungstic acid (PTA) was used as the NS-EM reagent; *ii*) TBS was the buffer; and *iii*) phospholipids were a major component of all the particles. We hypothesized that PTA in TBS mediates an interaction between the phospholipid molecules of adjacent lipoproteins to produce rouleau.

Role of PTA–phospholipid interactions in rouleau formation of liposome vesicles

To test whether it is the presence of lipids only that is sufficient for rouleau formation, we analyzed POPC liposome vesicles by using the conventional NS-EM protocol. EM micrographs revealed particles stacked into rouleau formation (**Fig. 1A**), suggesting that rouleau formation is due to the interaction between the POPC molecules of neighboring liposome vesicles (Fig. 1F). Similar results were also reported in earlier experiments with POPC and dimyristoyl phosphatidylcholine liposome vesicles, which formed stacks when PTA was used for NS-EM (44, 45).

Role of diluted buffer salt concentration in rouleau formation

Given that salts affect lipoprotein structure and induce neutral lipid membrane interactions (46, 47), we also examined the role of buffer salt concentration in rouleau formation. Even when samples were washed with deionized water prior to PTA staining, short rouleau appeared. Isolated particles were also observed under these conditions (21). Liposome vesicles from diluting buffer containing high (0.5 M NaCl) and low (0.1 M NaCl) slat concentrations and from buffer containing no salt (deionized water) were prepared and viewed by NS-EM. At 0.5 M NaCl, particles stacked together tightly in a fingerprint-like pattern (Fig. 1B). Stacking was also observed with low-salt concentration (0.1 M) and with no NaCl (Fig. 1C, D), but the rouleau contained fewer particles, suggesting that higher salt concentrations increased the interaction between POPC molecules of neighboring vesicles. Similar results were obtained with 9.6-nm apoA-I rHDL (data not shown) and apoE4 rHDL (21). In contrast, application of the optimized NS-EM protocol (21) to POPC liposomal vesicles revealed individual particles (Fig. 1E) which did not stack into rouleau, suggesting that this protocol may be suitable for POPC-containing rHDL.

Morphology and structure of rHDL

To test whether the optimized NS-EM protocol is suitable for visualizing different apoA-I-containing rHDL subclasses, we examined discoidal apoA-I rHDL (diameters of 9.6, 8.4, and 7.8 nm) and spherical rHDL (diameter, 9.3 nm).

The 9.6-nm discoidal rHDL samples appeared as flattened oval discs without rouleau. The high-density profile near the particle's edge, corresponding to the location of apoA-I in most models of rHDL, is fixed by a layer of heavy metal ions with negative stain in an emulsion of high ionic strength (33, 48). The central region of the particle appeared as a lower density hollow (**Fig. 2A,** left and middle panels). Analysis of the geometric mean of longest diameter and its orthogonal diameter (representing size) and their aspect ratio (representing shape) showed that ~90% of the selected 317 particles were 8–12 nm, with the peak population (~20.5%) at ~10.14 nm (Fig. 2F, left panel). The distribution of aspect ratios revealed shape heterogeneity and a generally oval-shaped discoidal morphology; ~90% of particle ratios were 1.0–1.6 nm, and the peak population (~21.2%) had an aspect ratio of 1.11 (Fig. 2F, right panel).

To reduce image noise and enhance clarity, a reference-free 2D class-averaging program (*refine2d.py* in EMAN software) was used to analyze particle variation. For classification and averaging, which are necessary for 3D reconstruction, we used a multivariate statistical analysis iterative classification scheme (22). Class averages showed that the 9.6-nm rHDL particles have a "Q" or "G" shape (Fig. 2A, right panel). The structural features are consistent with particles embedded in vitreous ice imaged by cryoEM (data not shown). The highest density was near the particle's edge (Fig. 2A, right and middle panels), with a small portion of density folded into the center of the disc. These high-contrast class averages with clean backgrounds are amenable to reconstruction of 3D density maps by the EM single-particle-reconstruction technique.

Electron micrographs of the 7.8-nm and 8.4-nm apoA-I rHDL also contained only isolated particles without rouleau (Fig. 2B, C). Computed geometric means and aspect ratios for 367 and 416 particles, respectively, showed that ~90% of the 7.8-nm rHDL particles were 6.5–9.5 nm in diameter, with the peak population (~22.3%) at ~7.93 nm; ~90% of the 8.4-nm rHDL particles were 7.0–10.0 nm, with the peak population (~23.2%) at ~8.55 nm. Approximately 90% of the 7.8-nm rHDL particles had an aspect ratio of 1.0–1.7, with the peak population (~17.3%) at 1.26. Ninety percent of the 8.4-nm rHDL particles had an aspect ratio of 1.0–1.9, with the peak population (~16.6%) at 1.55. This analysis suggests that particles of both subclasses were globular, with the 7.8-nm rHDL being ~18.7% smaller than the 8.4 nm rHDL. The 7.8 nm rHDL particles were nearly spherical, and the 8.4-nm rHDL particles were more ellipsoidal.

Reference-free class averaging algorithms generated high-contrast 2D class averages of 7.8-nm rHDL (Fig. 2B, right panel) and 8.4-nm rHDL (Fig. 2C, right panel). Class

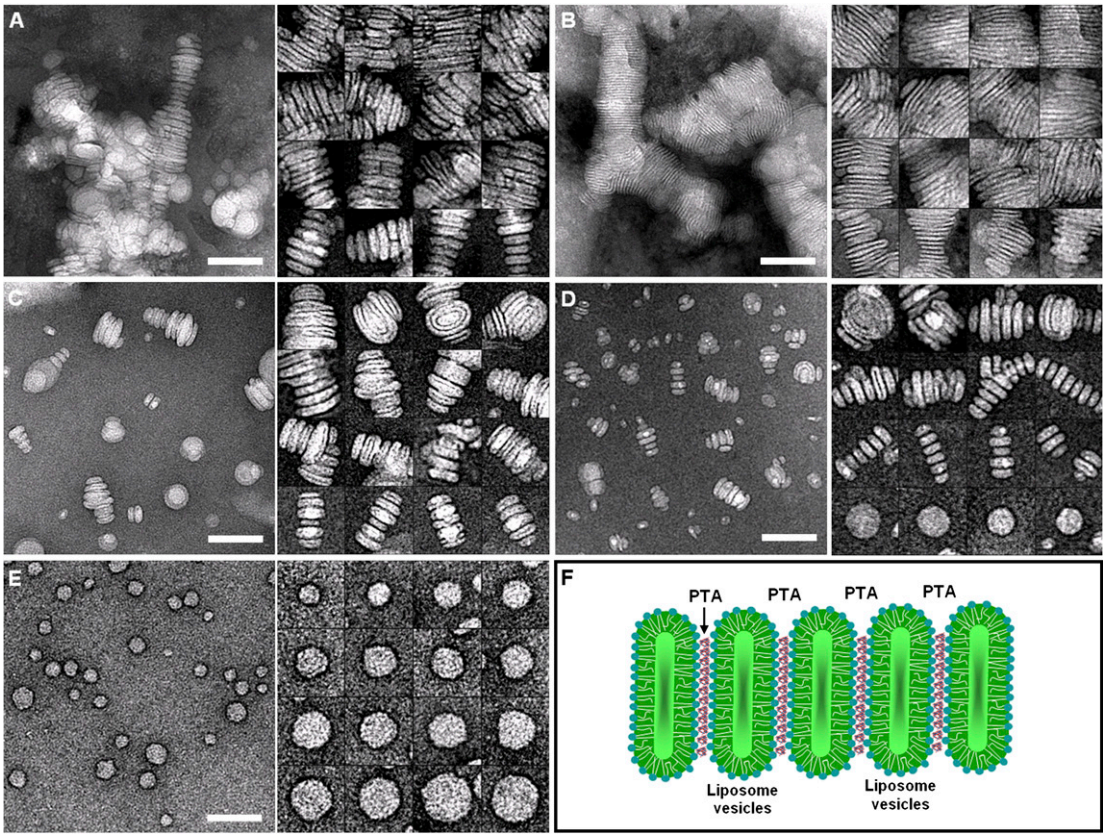

Fig. 1. Effects of staining method and salt concentration on rouleau formation in liposome vesicles. A: Liposome vesicles prepared with the conventional NS-EM method show a high degree of aggregation. B: High salt concentration leads to a higher degree of flattening and stacking. C: Low salt concentration causes less flattening and shorter rouleau. D: Even less flattening and stacking occurs with no salt. E: Liposome vesicles prepared with the optimized NS-EM method show well-isolated liposome particles. Left panels show a portion of the micrograph, whereas right panels show the enlarged views of windowed rouleau and individual liposome vesicles selected from NS-EM micrographs. F: A schematic presents the role of PTA in rouleau formation. Negative charges of PTA interact with the surface-positive charges of phospholipids (on the protonated amino groups of choline) and draw the amphipathic bilayers of different particles together to form rouleau. Bar = 100 nm; particle window size = 80 nm.

averages showed that particles of both subclasses had a high-density region resembling a figure 8 or figure 6 shape, with the high-density regions distributed near both the edge and the center (Fig. 2B, C). The high-contrast class averages with clean backgrounds also suggested that 7.8-nm rHDL and 8.4-nm rHDL samples are suitable for single-particle 3D reconstruction.

The 9.3-nm spherical rHDL, which appeared circular by NS-EM, varied in size (Fig. 2D). The geometric means (from 477 particles, total) exhibited size heterogeneity, with ~90% of particles between 8.5 and 12.0 nm and the peak population (~21.6%) at ~10.24 nm. The distribution of aspect ratios suggested a quasi-spherical morphology, with ~90% of particles having an aspect ratio between 1.0 and 1.4 and the peak population (~34.1%) having an aspect ratio of 1.11.

The NS-EM method may flatten particles during drying (49). However, statistical analysis of apoE4 rHDL particle sizes from cryoEM and optimized NS-EM data revealed a differential in particle size of less than 5% (21). To further test the degree of flattening due to the NS technique, we examined the 9.3-nm-diameter spherical rHDL sample by cryo-NS-EM (30, 50). The advantage of cryo-NS is that the particles are fixed by a negative stain layer of heavy metal ions in an emulsion of high ionic strength, meaning that the specimen can tolerate higher doses of electrons than in conventional cryoEM (50). The high electron dose increases the signal-to-noise ratio of images while maintaining specimen integrity (30, 50). The 9.3-nm spherical rHDL particles selected from cryo-NS micrographs showed circular shapes similar to those detected by NS-EM but with greater size variety (Fig. 2E). Analysis of cryo-NS particle size distribution for 300 particles confirmed that the particle features were similar to those observed by NS-EM, but the particles were 7.8% smaller, with ~90% of particles between 7.5 and 11.0 nm and the peak population (~19.1%) at ~9.44 nm. The distribution of aspect ratios also showed similar features, with 90% of particles having an aspect ratio of 1.0–1.5 and the peak population (~23.0%) at ~1.23. This analysis revealed that particle sizes and shapes measured by using NS-EM and cryo-NS micrographs were similar (less than 10% difference), suggesting that NS-EM is a reliable approach for analyzing lipoprotein structure and morphology.

To generate high-contrast 2D class averages, the detailed structure of 9.3-nm-diameter spherical rHDL as shown by NS-EM and cryo-NS-EM was analyzed using *refine2d.py* soft-

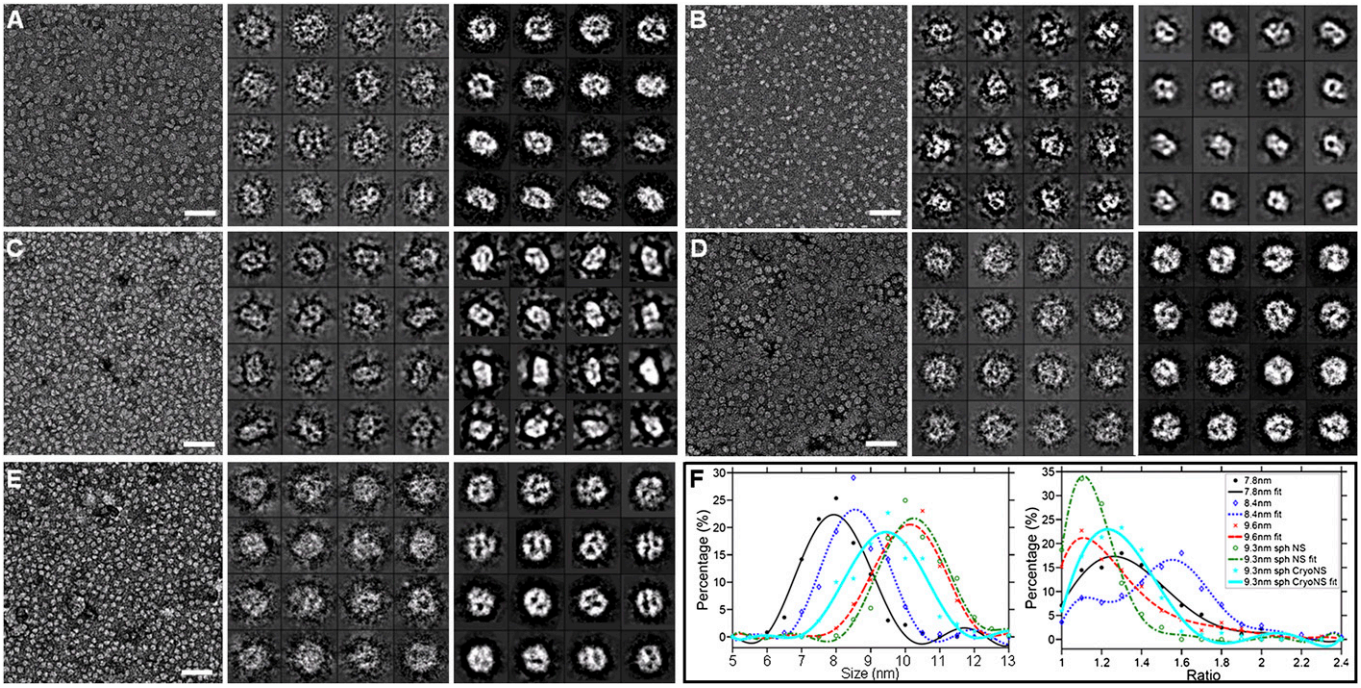

Fig. 2. Structure and morphology of apoA-I-containing rHDL samples prepared with the optimized NS-EM protocol using UF as the negative stain and DPBS as the diluting buffer. rHDL particles of various subclasses were isolated, and no rouleau were observed. Different subclasses are shown: (A) 9.6-nm rHDL; (B) 7.8-nm rHDL; (C) 8.4-nm rHDL; (D) 9.3-nm spherical rHDL; (E) 9.3-nm spherical rHDL by cryo-NS-EM. Left panels show a portion of the micrograph. Middle panels show selected 16 particles picked from the micrographs. Right panels show selected 16 class averages from a total of ~500 class averages that were, respectively, computed from the total of 9,703 particles of 9.6-nm rHDL; 6,841 particles of 8.4-nm rHDL; 5,578 particles of 7.8-nm rHDL; 17,441 particles of NS 9.3-nm spherical rHDL; and 5,386 particles of cryo-NS-EM 9.3-nm spherical rHDL. F: Distributions of particle size and shape are shown. Size was measured as the geometric mean (the square root of the product) of two perpendicular diameters and shape as the aspect ratio between these two perpendicular diameters. Bar = 50 nm; particle window size = 20 nm.

ware (22, 32). Class averages from NS-EM and cryo-NS-EM produced similar structural details, and both methods showed that the 9.3-nm rHDL particles were spherical (Fig. 2D, E) with contiguous high densities near the particle's edge and center. This similarity further suggests that the drying step in NS-EM has minimal effect on particle size and shape and validates the NS-EM protocol for more studies of lipoprotein structure.

Human plasma HDL morphology and structure

To test whether the optimized NS-EM protocol is effective for analysis of isolated human plasma HDL, we examined α-migrating HDL (**Fig. 3A, B**). Plasma HDL appeared as isolated globular particles that were heterogeneous in size. Sizes of selected 408 particles varied; ~90% of the particles were 9.0–15.0 nm in diameter (Fig. 3C).

Morphology and structure of human plasma LDL, IDL, and VLDL

To test the optimized NS-EM protocol with apoB-100-containing lipoproteins, human plasma LDL (subfraction 3), IDL, and VLDL were examined (**Fig. 4**). For LDL, only isolated particles without rouleau formation were visible. Approximately 90% of the selected 388 particles were 26.0–32.0 nm in diameter, with the peak population (~22.6%) at ~28.4 nm (Fig. 4D, left panel). The histogram of the aspect ratios suggested a generally spherical morphology. In detail, ~90% of the particles had aspect ratios of 1.00–1.30, with the peak population (~19.0%) having an aspect ratio at ~1.14 (Fig. 4D, right panel).

Similarly, electron micrographs of IDL and VLDL showed no rouleau formation. Most (~90%) of the selected 218 IDL particles were 26.0–50.0 nm in diameter, and ~90% of the selected 222 VLDL particles were 30.0–60.0 nm (Fig. 4B, C). As expected, VLDL particles were larger than IDL particles (Fig. 4D). The peak population (~4.5%) of VLDL particles occurred at 40.6 nm (Fig. 4D), ~12.6% larger than the peak population size of IDL (36.10 nm) (Fig. 4D). According to the distribution of aspect ratios, most VLDL particles were spherical, with ~90% having an aspect ratio of 1.00–1.25, and the aspect ratio of the peak population was 1.05. IDL particle shape was more variable, with ~90% of the particles having an aspect ratio of 1.00–1.50, a range ~100% wider than that of VLDL, suggesting that IDL is more flexible and dynamic than VLDL.

VLDL and IDL particles exhibited much more size and shape heterogeneity than LDL particles (Fig. 4), consistent with a large compositional variability. According to their aspect ratios, both VLDL and IDL particles are quasi-spherical (Fig. 4D). Moreover, IDL particles exhibited wavy, crenellated surfaces (Fig. 4B). The underlying cause for this unusual shape is most likely that IDL are smaller

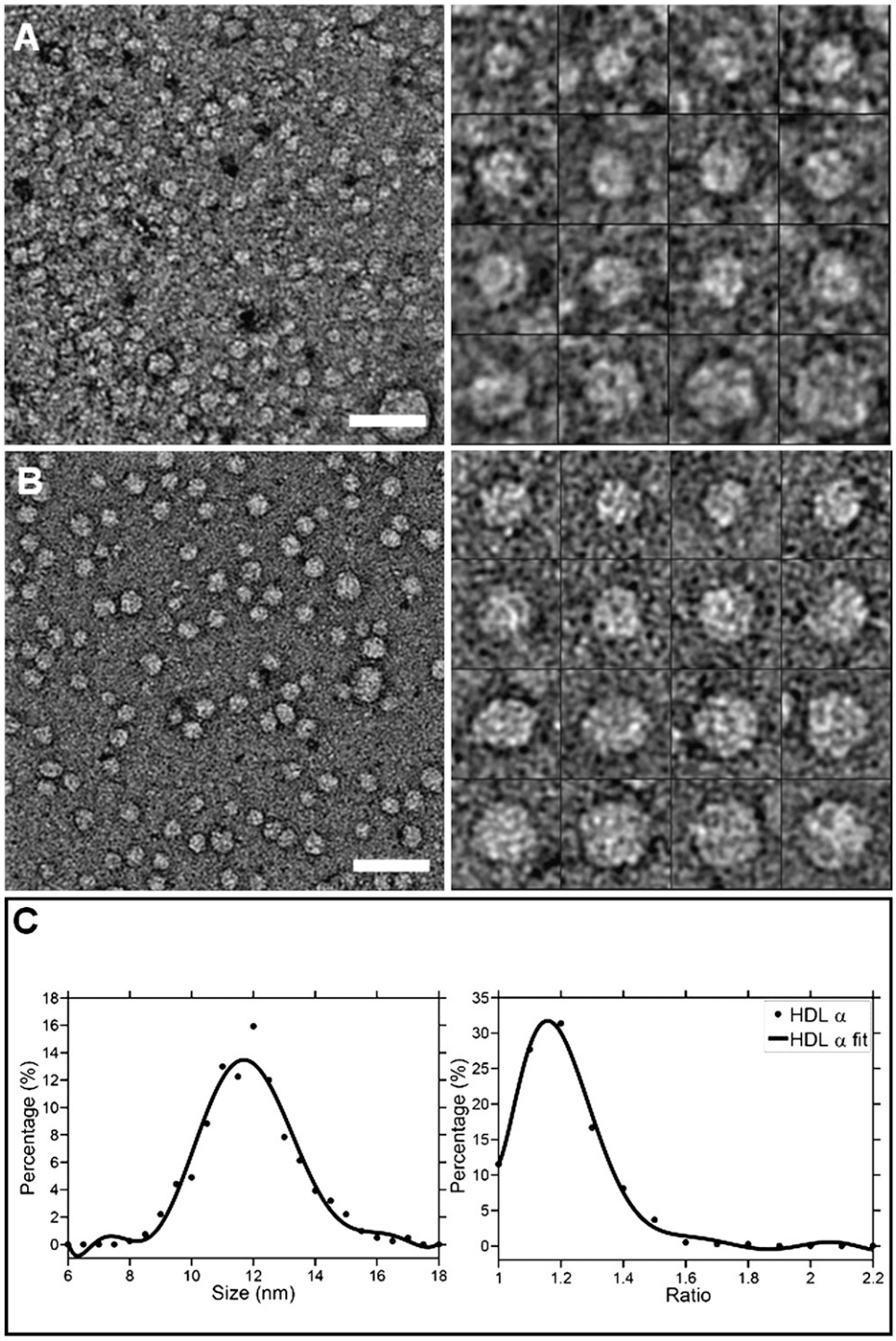

Fig. 3. Structure and morphology of human plasma HDL subjected to optimized NS treatment. A: Mixture of all subclasses is shown. B: α HDL. Micrographs (left panel) and selected individual HDL particles (right panel) are shown. C: Particle size and shape distribution of alpha HDL. Size was measured as the geometric mean of two perpendicular diameters and shape as the aspect ratio between them. Bar = 50 nm; particle window size = 25 nm.

than VLDL but they have similar amounts of surface lipids that rearrange into "folds" in order to be accommodated on the particle's surface (51–55). It is also possible that the uneven surface of IDL may be due to the accumulation of fatty acids produced by the lipolytic removal of the triglyceride core. While most of these fatty acids transfer to albumin under physiological conditions, some phospholipids as well as apoB and apoE remain associated with the particle surface. As these surface constituents now surround a much smaller post-lipolytic particle, the folds may be caused by compression of the surface monolayer subsequent to particle shrinkage.

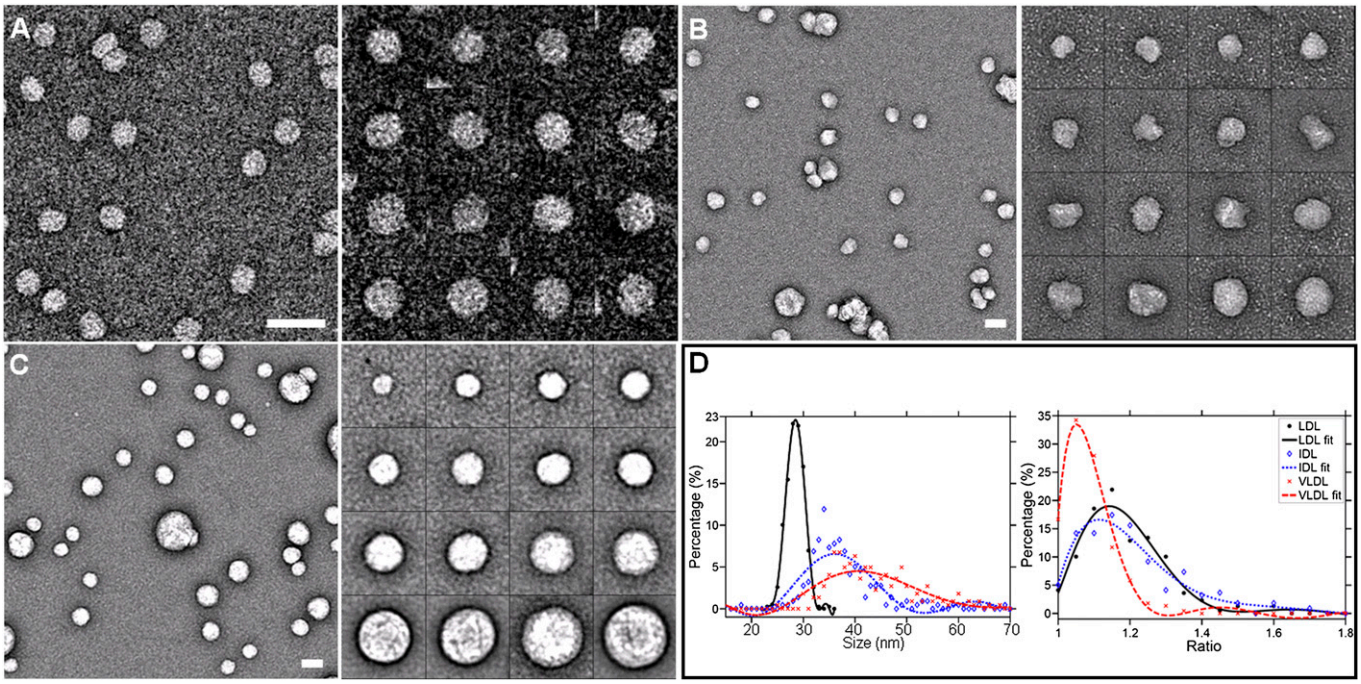

Fig. 4. Structure and morphology of human plasma apoB-100 lipoproteins prepared by the optimized NS method. LDL (subfraction 3) (A), IDL (B), and VLDL (C) particles were all well isolated, and no rouleau formation was observed. Micrographs (left panel) and selected individual particles (right panel) are shown for each lipoprotein class/fraction. D: Particle size and shape distributions. Size was measured as the geometric mean of two perpendicular diameters and shape as the aspect ratio between them. Bar = 50 nm; particle window size = 100 nm, except in panel A, where box = 50 nm.

DISCUSSION

We have examined the effects of PTA and salt concentrations on the morphology of liposome vesicles observed by NS-EM and discovered that PTA mediates phospholipid–phospholipid interactions that induce rouleau formation in lipid-related particles such as apoA-I rHDL and apoB-100 LDL. Tests of our new protocol validated the use of PTA on other lipoproteins with no evidence of rouleau formation.

PTA and uranyl stains are widely used in the imaging of biological samples by EM (29, 48, 56, 57). However, PTA-stained lipoproteins, phospholipids, bile acids, phospholipid-cholesterol liposome vesicles, lipid vesicles, and bilayer membranes frequently appear as disc-shaped particles stacked into rouleau (58-62). This stacking likely occurs through the association of multiple negative charges of PTA with the positive surface charge of phospholipids (the protonated choline amino groups), forcing the amphipathic bilayers of different particles into rouleau (Fig. 1F). This is consistent with the use of PTA or $MgCl_2$ as a means of precipitating HDL from serum (63).

Unlike PTA, uranyl stains are cationic and do not associate electrostatically with positively charged phospholipids (21). In contrast to PTA staining (pH 7.4), UF staining is performed at pH 4.6. If pH level contributes to rouleau formation, UF should be more likely to form rouleau than PTA because the pH of PTA is closer to that of lipoproteins (pH 7.4). However, uranyl-stained samples do not produce rouleau, suggesting that pH is not a factor for stacking into rouleau. An additional advantage of uranyl stains is that the grain size is finer (diameter, ~0.3 nm) than that of PTA (diameter, ~0.8–0.9 nm; grain size, ~1.2 nm) (64–66) and therefore gives better details (33). This is important for particles whose molecular mass is less than 100 kDa (33). The fine structural details of lipoproteins stained in the optimized NS-EM protocol verify that this approach yields images that are amenable to high-resolution 3D reconstructions of lipoprotein particles.

The mechanism by which UF and PTA interact with phosphocholine is not clear. UF fixes protein structure on a millisecond timescale (67) so that mildly acidic pH, 4.2–4.6, should not be lipolytic. The choline group contains a positive charge, whereas the phosphoryl moiety is negatively charged, giving its well-known zwitterionic structure. The mechanism of PTA adsorption to surfaces is electrostatic, rather than via hydrogen bonding, because adsorption was not affected by pH (68). In contrast to PTA, UF is a salt, not an acid. As far as we know, using UF, lipoprotein particles were all displayed in isolated form (62, 69, 70).

The 9.6-nm rHDL particles have been used as models to determine the structure of apoA-I in nascent HDL (2, 71–77). Despite debate about details, most recent theoretical and experimental data support a discoidal shape, including the "looped belt" and "solar flare" models (73-79). In most discoidal models, two apoA-I molecules associate in an antiparallel orientation and circumscribe a phospholipid bilayer (2, 72-74, 80, 81). Reference-free class averages of 9.6-nm rHDL particles show a cable-like high-density

ring contiguous with a small high-density penetrating disc center (Fig. 2A, right panel). Despite difference in details, the overall shape of 9.6-nm rHDL is consistent with that of the discoidal models.

In summary, our proposed optimized NS-EM protocol is suitable for exploring the morphology and structural details of lipoprotein classes and their subclasses/subspecies.

We thank Drs. Jianjun Wang, Jere P. Segrest, and Ling Li for providing rHDL samples for initial testing and Dr. Richard J. Havel and Jere P. Segrest for comments on the manuscript.

REFERENCES

1. Havel, R. J., J. L. Goldstein, and M. S. Brown. 1980. Lipoproteins and lipid transport. *In* The Metabolic Control of Disease. P. B. a. L. Rosenberg, editor. W.B. Saunders Co., Philadelphia. 398–399.
2. Silva, R. A., R. Huang, J. Morris, J. Fang, E. O. Gracheva, G. Ren, A. Kontush, W. G. Jerome, K. A. Rye, and W. S. Davidson. 2008. Structure of apolipoprotein A-I in spherical high density lipoproteins of different sizes. *Proc. Natl. Acad. Sci. U S A.* **105:** 12176–12181.
3. Fredrickson, D. S., R. I. Levy, and R. S. Lees. 1967. Fat transport in lipoproteins–an integrated approach to mechanisms and disorders. *N. Engl. J. Med.* 276: 273–281.
4. van Antwerpen, R., M. La Belle, E. Navratilova, and R. M. Krauss. 1999. Structural heterogeneity of apoB-containing serum lipoproteins visualized using cryo-electron microscopy. *J. Lipid Res.* **40:** 1827–1836.
5. Ren, G., G. Rudenko, S. J. Ludtke, J. Deisenhofer, W. Chiu, and H. J. Pownall. 2010. Model of human low-density lipoprotein and bound receptor based on cryoEM. *Proc. Natl. Acad. Sci. U S A.* **107:** 1059–1064.
6. Austin, M. A. 1994. Small, dense low-density lipoprotein as a risk factor for coronary heart disease. *Int. J. Clin. Lab. Res.* **24:** 187–192.
7. Rudenko, G., L. Henry, K. Henderson, K. Ichtchenko, M. S. Brown, J. L. Goldstein, and J. Deisenhofer. 2002. Structure of the LDL receptor extracellular domain at endosomal pH. *Science.* **298:** 2353–2358.
8. van Antwerpen, R., G. C. Chen, C. R. Pullinger, J. P. Kane, M. LaBelle, R. M. Krauss, C. Luna-Chavez, T. M. Forte, and J. C. Gilkey. 1997. Cryo-electron microscopy of low density lipoprotein and reconstituted discoidal high density lipoprotein: imaging of the apolipoprotein moiety. *J. Lipid Res.* **38:** 659–669.
9. Xu, Y., and M. Fu. 2003. Alterations of HDL subclasses in hyperlipidemia. *Clin. Chim. Acta.* 332: 95–102.
10. Bodzioch, M., E. Orso, J. Klucken, T. Langmann, A. Bottcher, W. Diederich, W. Drobnik, S. Barlage, C. Buchler, M. Porsch-Ozcurumez, et al. 1999. The gene encoding ATP-binding cassette transporter 1 is mutated in Tangier disease. *Nat. Genet.* **22:** 347–351.
11. Jonas, A. 1998. Regulation of lecithin cholesterol acyltransferase activity. *Prog. Lipid Res.* **37:** 209–234.
12. Xu, S., M. Laccotripe, X. Huang, A. Rigotti, V. I. Zannis, and M. Krieger. 1997. Apolipoproteins of HDL can directly mediate binding to the scavenger receptor SR-BI, an HDL receptor that mediates selective lipid uptake. *J. Lipid Res.* **38:** 1289–1298.
13. Rye, K. A., R. Bright, M. Psaltis, and P. J. Barter. 2006. Regulation of reconstituted high density lipoprotein structure and remodeling by apolipoprotein E. *J. Lipid Res.* **47:** 1025–1036.
14. Cavigiolio, G., B. Shao, E. G. Geier, G. Ren, J. W. Heinecke, and M. N. Oda. 2008. The interplay between size, morphology, stability, and functionality of high-density lipoprotein subclasses. *Biochemistry.* **47:** 4770–4779.
15. Jeyarajah, E. J., W. C. Cromwell, and J. D. Otvos. 2006. Lipoprotein particle analysis by nuclear magnetic resonance spectroscopy. *Clin. Lab. Med.* **26:** 847–870.
16. Otvos, J. D., E. J. Jeyarajah, and W. C. Cromwell. 2002. Measurement issues related to lipoprotein heterogeneity. *Am. J. Cardiol.* **90:** 22i–29i.
17. Oda, M. N., T. M. Forte, R. O. Ryan, and J. C. Voss. 2003. The C-terminal domain of apolipoprotein A-I contains a lipid-sensitive conformational trigger. *Nat. Struct. Biol.* **10:** 455–460.
18. Davidson, W. S., and R. A. Silva. 2005. Apolipoprotein structural organization in high density lipoproteins: belts, bundles, hinges and hairpins. *Curr. Opin. Lipidol.* **16:** 295–300.
19. Wu, Z., M. A. Wagner, L. Zheng, J. S. Parks, J. M. Shy III, J. D. Smith, V. Gogonea, and S. L. Hazen. 2007. The refined structure of nascent HDL reveals a key functional domain for particle maturation and dysfunction. *Nat. Struct. Mol. Biol.* **14:** 861–868.
20. Orlova, E. V., M. B. Sherman, W. Chiu, H. Mowri, L. C. Smith, and A. M. Gotto, Jr. 1999. Three-dimensional structure of low density lipoproteins by electron cryomicroscopy. *Proc. Natl. Acad. Sci. U S A.* 96: 8420–8425.
21. Zhang, L., J. Song, Y. Newhouse, S. Zhang, K. H. Weisgraber, and G. Ren. 2010. An optimized negative-staining protocol of electron microscopy for apoE4 POPC lipoprotein. *J. Lipid Res.* **51:** 1228–1236.
22. Ludtke, S. J., P. R. Baldwin, and W. Chiu. 1999. EMAN: semiautomated software for high-resolution single-particle reconstructions. *J. Struct. Biol.* **128:** 82–97.
23. Frank, J., M. Radermacher, P. Penczek, J. Zhu, Y. Li, M. Ladjadj, and A. Leith. 1996. SPIDER and WEB: processing and visualization of images in 3D electron microscopy and related fields. *J. Struct. Biol.* **116:** 190–199.
24. Ryan, R. O., T. M. Forte, and M. N. Oda. 2003. Optimized bacterial expression of human apolipoprotein A-I. *Protein Expr. Purif.* **27:** 98–103.
25. Rye, K. A., N. J. Hime, and P. J. Barter. 1995. The influence of cholesteryl ester transfer protein on the composition, size, and structure of spherical, reconstituted high density lipoproteins. *J. Biol. Chem.* **270:** 189–196.
26. Rye, K. A., K. H. Garrety, and P. J. Barter. 1993. Preparation and characterization of spheroidal, reconstituted high-density lipoproteins with apolipoprotein A-I only or with apolipoprotein A-I and A-II. *Biochim. Biophys. Acta.* **1167:** 316–325.
27. O'Connor, P. M., B. R. Zysow, S. A. Schoenhaus, B. Y. Ishida, S. T. Kunitake, J. M. Naya-Vigne, P. N. Duchateau, R. F. Redberg, S. J. Spencer, S. Mark, et al. 1998. Prebeta-1 HDL in plasma of normolipidemic individuals: influences of plasma lipoproteins, age, and gender. *J. Lipid Res.* **39:** 670–678.
28. Chen, H. H., B. D. Hosken, M. Huang, J. W. Gaubatz, C. L. Myers, R. D. Macfarlane, H. J. Pownall, and C. Y. Yang. 2007. Electronegative LDLs from familial hypercholesterolemic patients are physicochemically heterogeneous but uniformly proapoptotic. *J. Lipid Res.* **48:** 177–184.
29. Forte, T. M., and L. A. Carlson. 1984. Electron microscopic structure of serum lipoproteins from patients with fish eye disease. *Arteriosclerosis.* 4: 130–137.
30. De Carlo, S., C. Carles, M. Riva, and P. Schultz. 2003. Cryo-negative staining reveals conformational flexibility within yeast RNA polymerase I. *J. Mol. Biol.* **329:** 891–902.
31. Grigorieff, N. 2007. FREALIGN: high-resolution refinement of single particle structures. *J. Struct. Biol.* **157:** 117–125.
32. Tang, G., L. Peng, P. R. Baldwin, D. S. Mann, W. Jiang, I. Rees, and S. J. Ludtke. 2007. EMAN2: an extensible image processing suite for electron microscopy. *J. Struct. Biol.* **157:** 38–46.
33. Ohi, M., Y. Li, Y. Cheng, and T. Walz. 2004. Negative staining and image classification —powerful tools in modern electron microscopy. *Biol. Proced. Online.* **6:** 23–34.
34. Forte, T., K. R. Norum, J. A. Glomset, and A. V. Nichols. 1971. Plasma lipoproteins in familial lecithin: cholesterol acyltransferase deficiency: structure of low and high density lipoproteins as revealed by elctron microscopy. *J. Clin. Invest.* **50:** 1141–1148.
35. Forte, T. M., and R. W. Nordhausen. 1986. Electron microscopy of negatively stained lipoproteins. *Methods Enzymol.* **128:** 442–457.
36. Gong, E. L., A. V. Nichols, K. H. Weisgraber, T. M. Forte, V. G. Shore, and P. J. Blanche. 1989. Discoidal complexes containing apolipoprotein E and their transformation by lecithin-cholesterol acyltransferase. *Biochim. Biophys. Acta.* **1006:** 317–328.
37. Schneeweis, L. A., V. Koppaka, S. Lund-Katz, M. C. Phillips, and P. H. Axelsen. 2005. Structural analysis of lipoprotein E particles. *Biochemistry.* **44:** 12525–12534.
38. Raussens, V., J. Drury, T. M. Forte, N. Choy, E. Goormaghtigh, J. M. Ruysschaert, and V. Narayanaswami. 2005. Orientation and mode of lipid-binding interaction of human apolipoprotein E C-terminal domain. *Biochem. J.* **387:** 747–754.
39. Li, X., H. Y. Kan, S. Lavrentiadou, M. Krieger, and V. Zannis. 2002. Reconstituted discoidal ApoE-phospholipid particles are ligands for the scavenger receptor BI. The amino-terminal 1–165 domain of ApoE suffices for receptor binding. *J. Biol. Chem.* **277:** 21149–21157.

40. Innerarity, T. L., R. E. Pitas, and R. W. Mahley. 1979. Binding of arginine-rich (E) apoprotein after recombination with phospholipid vesicles to the low density lipoprotein receptors of fibroblasts. *J. Biol. Chem.* **254:** 4186–4190.
41. Lu, B., J. A. Morrow, and K. H. Weisgraber. 2000. Conformational reorganization of the four-helix bundle of human apolipoprotein E in binding to phospholipid. *J. Biol. Chem.* **275:** 20775–20781.
42. van Antwerpen, R. 2004. Preferred orientations of LDL in vitreous ice indicate a discoid shape of the lipoprotein particle. *Arch. Biochem. Biophys.* **432:** 122–127.
43. Peters-Libeu, C. A., Y. Newhouse, D. M. Hatters, and K. H. Weisgraber. 2006. Model of biologically active apolipoprotein E bound to dipalmitoylphosphatidylcholine. *J. Biol. Chem.* **281:** 1073–1079.
44. Melchior, V., C. J. Hollingshead, and M. E. Cahoon. 1980. Stacking in lipid vesicle-tubulin mixtures is an artifact of negative staining. *J. Cell Biol.* **86:** 881–884.
45. Guo, L. S., R. L. Hamilton, J. Goerke, J. N. Weinstein, and R. J. Havel. 1980. Interaction of unilamellar liposomes with serum lipoproteins and apolipoproteins. *J. Lipid Res.* **21:** 993–1003.
46. Petrache, H. I., T. Zemb, L. Belloni, and V. A. Parsegian. 2006. Salt screening and specific ion adsorption determine neutral-lipid membrane interactions. *Proc. Natl. Acad. Sci. U S A.* **103:** 7982–7987.
47. Jayaraman, S., D. L. Gantz, and O. Gursky. 2006. Effects of salt on the thermal stability of human plasma high-density lipoprotein. *Biochemistry.* **45:** 4620–4628.
48. Oliver, R. M. 1973. Negative stain electron microscopy of protein macromolecules. *Methods Enzymol.* **27:** 616–672.
49. Cheng, Y., E. Wolf, M. Larvie, O. Zak, P. Aisen, N. Grigorieff, S. C. Harrison, and T. Walz. 2006. Single particle reconstructions of the transferrin-transferrin receptor complex obtained with different specimen preparation techniques. *J. Mol. Biol.* **355:** 1048–1065.
50. Adrian, M., J. Dubochet, S. D. Fuller, and J. R. Harris. 1998. Cryo-negative staining. *Micron.* **29:** 145–160.
51. Williams, P. T., R. M. Krauss, P. D. Wood, F. T. Lindgren, C. Giotas, and K. M. Vranizan. 1986. Lipoprotein subfractions of runners and sedentary men. *Metabolism.* **35:** 45–52.
52. Krauss, R. M., and D. J. Burke. 1982. Identification of multiple subclasses of plasma low density lipoproteins in normal humans. *J. Lipid Res.* **23:** 97–104.
53. Tatami, R., H. Mabuchi, K. Ueda, R. Ueda, T. Haba, T. Kametani, S. Ito, J. Koizumi, M. Ohta, S. Miyamoto, et al. 1981. Intermediate-density lipoprotein and cholesterol-rich very low density lipoprotein in angiographically determined coronary artery disease. *Circulation.* **64:** 1174–1184.
54. Krauss, R. M., F. T. Lindgren, P. T. Williams, S. F. Kelsey, J. Brensike, K. Vranizan, K. M. Detre, and R. I. Levy. 1987. Intermediate-density lipoproteins and progression of coronary artery disease in hypercholesterolaemic men. *Lancet.* **2:** 62–66.
55. Hodis, H. N., W. J. Mack, M. Dunn, C. Liu, C. Liu, R. H. Selzer, and R. M. Krauss. 1997. Intermediate-density lipoproteins and progression of carotid arterial wall intima-media thickness. *Circulation.* **95:** 2022–2026.
56. Ohtsuki, M., C. Edelstein, M. Sogard, and A. M. Scanu. 1977. Electron microscopy of negatively stained and freeze-etched high density lipoprotein-3 from human serum. *Proc. Natl. Acad. Sci. U S A.* **74:** 5001–5005.
57. Leberman, R. 1965. Use of uranyl formate as a negative stain. *J. Mol. Biol.* **13:** 606–611.
58. Thrift, R. N., T. M. Forte, B. E. Cahoon, and V. G. Shore. 1986. Characterization of lipoproteins produced by the human liver cell line, Hep G2, under defined conditions. *J. Lipid Res.* **27:** 236–250.
59. Forte, T. M., C. E. Cross, R. A. Gunther, and G. C. Kramer. 1983. Characterization of sheep lung lymph lipoproteins: chemical and physical properties. *J. Lipid Res.* **24:** 1358–1367.
60. Swaney, J. B. 1983. Reconstitution of apolipoprotein A-I from human high density lipoprotein with bovine brain sphingomyelin. *J. Biol. Chem.* **258:** 1254–1259.
61. Musliner, T. A., M. D. Long, T. M. Forte, A. V. Nichols, E. L. Gong, P. J. Blanche, and R. M. Krauss. 1991. Dissociation of high density lipoprotein precursors from apolipoprotein B-containing lipoproteins in the presence of unesterified fatty acids and a source of apolipoprotein A-I. *J. Lipid Res.* **32:** 917–933.
62. Chen, B., X. Ren, T. Neville, W. G. Jerome, D. W. Hoyt, D. Sparks, G. Ren, and J. Wang. 2009. Apolipoprotein AI tertiary structures determine stability and phospholipid-binding activity of discoidal high-density lipoprotein particles of different sizes. *Protein Sci.* **18:** 921–935.
63. Schmitz, G., and G. Assmann. 1982. Isolation of human serum HDL1 by zonal ultracentrifugation. *J. Lipid Res.* **23:** 903–910.
64. Hayat, M. A. 2000. Negative stains. *In* Principles and Techniques Of Electron Microscopy: biological applications. Cambridge University Press, NY. 372–377.
65. Harris, J. R., W. Gebauer, S. M. Sohngen, M. V. Nermut, and J. Markl. 1997. Keyhole limpet hemocyanin (KLH), II: Characteristic reassociation properties of purified KLH1 and KLH2. *Micron.* **28:** 43–56.
66. Harris, J. R., W. Gebauer, F. U. Guderian, and J. Markl. 1997. Keyhole limpet hemocyanin (KLH), I: Reassociation from Immucothel followed by separation of KLH1 and KLH2. *Micron.* **28:** 31–41.
67. Zhao, F. Q., and R. Craig. 2003. Capturing time-resolved changes in molecular structure by negative staining. *J. Struct. Biol.* **141:** 43–52.
68. Quintarelli, G., R. Zito, and J. A. Cifonelli. 1971. On phosphotungstic acid staining. I. *J. Histochem. Cytochem.* **19:** 641–647.
69. Whorton, M. R., B. Jastrzebska, P. S. Park, D. Fotiadis, A. Engel, K. Palczewski, and R. K. Sunahara. 2008. Efficient coupling of transducin to monomeric rhodopsin in a phospholipid bilayer. *J. Biol. Chem.* **283:** 4387–4394.
70. Jenne, D. E., B. Lowin, M. C. Peitsch, A. Bottcher, G. Schmitz, and J. Tschopp. 1991. Clusterin (complement lysis inhibitor) forms a high density lipoprotein complex with apolipoprotein A-I in human plasma. *J. Biol. Chem.* **266:** 11030–11036.
71. Wu, Z., V. Gogonea, X. Lee, M. A. Wagner, X. M. Li, Y. Huang, A. Undurti, R. P. May, M. Haertlein, M. Moulin, et al. 2009. Double superhelix model of high density lipoprotein. *J. Biol. Chem.* **284:** 36605–36619.
72. Segrest, J. P., L. Li, G. M. Anantharamaiah, S. C. Harvey, K. N. Liadaki, and V. Zannis. 2000. Structure and function of apolipoprotein A-I and high-density lipoprotein. *Curr. Opin. Lipidol.* **11:** 105–115.
73. Gu, F., M. K. Jones, J. Chen, J. C. Patterson, A. Catte, W. G. Jerome, L. Li, and J. P. Segrest. 2010. Structures of discoidal high density lipoproteins: a combined computational-experimental approach. *J. Biol. Chem.* **285:** 4652–4665.
74. Martin, D. D., M. S. Budamagunta, R. O. Ryan, J. C. Voss, and M. N. Oda. 2006. Apolipoprotein A-I assumes a "looped belt" conformation on reconstituted high density lipoprotein. *J. Biol. Chem.* **281:** 20418–20426.
75. Segrest, J. P., M. K. Jones, A. E. Klon, C. J. Sheldahl, M. Hellinger, H. De Loof, and S. C. Harvey. 1999. A detailed molecular belt model for apolipoprotein A-I in discoidal high density lipoprotein. *J. Biol. Chem.* **274:** 31755–31758.
76. Li, H., D. S. Lyles, M. J. Thomas, W. Pan, and M. G. Sorci-Thomas. 2000. Structural determination of lipid-bound ApoA-I using fluorescence resonance energy transfer. *J. Biol. Chem.* **275:** 37048–37054.
77. Thomas, M. J., S. Bhat, and M. G. Sorci-Thomas. 2008. Three-dimensional models of HDL apoA-I: implications for its assembly and function. *J. Lipid Res.* **49:** 1875–1883.
78. Tricerri, M. A., A. K. Behling Agree, S. A. Sanchez, J. Bronski, and A. Jonas. 2001. Arrangement of apolipoprotein A-I in reconstituted high-density lipoprotein disks: an alternative model based on fluorescence resonance energy transfer experiments. *Biochemistry.* **40:** 5065–5074.
79. Shih, A. Y., I. G. Denisov, J. C. Phillips, S. G. Sligar, and K. Schulten. 2005. Molecular dynamics simulations of discoidal bilayers assembled from truncated human lipoproteins. *Biophys. J.* **88:** 548–556.
80. Hamilton, R. L., M. C. Williams, C. J. Fielding, and R. J. Havel. 1976. Discoidal bilayer structure of nascent high density lipoproteins from perfused rat liver. *J. Clin. Invest.* **58:** 667–680.
81. Felker, T. E., R. L. Hamilton, and R. J. Havel. 1978. Secretion of lipoprotein-X by perfused livers of rats with cholestasis. *Proc. Natl. Acad. Sci. U S A.* **75:** 3459–3463.